



# Experimental investigation on high-shear and low-pressure grinding process for Inconel718 superalloy

Yebing Tian<sup>1,2</sup> · Linguang Li<sup>1</sup> · Bing Liu<sup>1</sup> · Jinguo Han<sup>1,2</sup> · Zenghua Fan<sup>1,2</sup>

Received: 27 September 2019 / Accepted: 31 March 2020 / Published online: 16 April 2020  
© Springer-Verlag London Ltd., part of Springer Nature 2020

## Abstract

In this work, we reported a novel grinding method with high tangential grinding force and low normal grinding force using specially developed grinding tools. The tools were made of flexible composites based on the principle of liquid body armor and the shear thickening mechanism of non-Newtonian fluid. During grinding, abrasive particles are capable of generating a “hydro-cluster effects” under reverse tangential load, which lead to the decreased normal grinding force and the increased tangential grinding force. Hence, workpiece materials are removed under “high-shear and low-pressure” grinding mode. A serial of grinding experiments were carried out on Inconel718. The results showed that the novel grinding tool had an excellent grinding performance on Inconel718 workpieces. The value of surface roughness decreased from  $Ra$  473.7 nm to  $Ra$  153.0 nm under the optimal grinding parameters, i.e., wheel speed of 1 m/s, workpiece speed of 2000 mm/min, and grinding depth of cut of 180  $\mu$ m. The surface defects of the Inconel718 workpiece were gradually removed. Meanwhile, the uniformed grinding textures were generated. The surface of the grinding tool had residual wear debris, and there was a little loss of grains after 240 grinding cycles.

**Keywords** Flexible composites · Grinding tools · High-shear and low-pressure grinding · Precision grinding · Nickel-based superalloy

## 1 Introduction

Nickel-based superalloys (i.e., GH333, Inconel718, and Inconel738) not only have excellent high-temperature strength, oxidation resistance, corrosion resistance, thermal stability, and thermal fatigue resistance performance, but also possess high working reliability. They are capable of handling complex stresses even under oxidation and gas corrosion conditions of over 650 °C [1–4]. Therefore, nickel-based superalloys, as the materials of key parts and components, have been widely utilized in the fields of aerospace engine turbine, turboprop, and turbine shaft, etc. As nickel-based superalloy parts suffer from the corrosive medium and alternating load

for a long time, their poor surface integrity would accelerate the fatigue damage of parts and reduce the service life. Hence, subsequent finishing processing is required [5–7].

Nowadays, grinding is one of the most critical surface finishing processes to meet desired part requirements for difficult-to-machine materials in manufacturing industries [8–11]. Nickel-based superalloys as a typical difficult-to-machine material have some challenges in the process of grinding, such as high grinding temperature, easy adhesion of grinding wheel, low material removal rate, and poor surface integrity of workpiece [12–14]. In recent years, a large number of experimental and theoretical investigations have been conducted to improve the machinability of nickel-based superalloys in the precision grinding. For example, Dai et al. [15] investigated the effects of diamond grain cutting-edges morphology and grinding wheel speed on grinding performance of Inconel718 in terms of grinding force, scratching mechanism, and specific grinding energy of a single diamond grain of different shapes. Bhaduri et al. [16] explored the effects of ultrasonic vibration with an open structured alumina-based grinding wheel during creep feed grinding for Inconel718. It was demonstrated that ultrasonic vibration increased the number of active cutting points on the grinding wheel. Yao et al.

✉ Yebing Tian  
tianyeb@sdu.edu.cn; tyb79@sina.com

<sup>1</sup> School of Mechanical Engineering, Shandong University of Technology, 266 Xincun West Road, Zibo 255049, People's Republic of China

<sup>2</sup> Institute for Advanced Manufacturing, Shandong University of Technology, Zibo 255049, People's Republic of China

[17] investigated the surface integrity of Inconel718 during the grinding process with a resin cubic boron nitride (CBN) wheel and a vitrified bond alumina wheel. The effects of grinding parameters on grinding force, temperature, and surface integrity were explored. Gong et al. [18] established a prediction model to predict the tangential grinding force and the normal grinding force. Influence of grinding parameters on grinding force, surface roughness, surface microstructure, and subsurface damage was analyzed.

At the same time, many types of novel grinding tools have also been developed and fabricated for the grinding of superalloys (e.g., monolayer brazed wheel, slotted grinding wheel, and diamond whisker wheel) [19–21]. Li et al. [19] developed a novel brazing technique—continuous induction brazing technique, to prepare a cubic boron nitride (CBN) single brazing grinding wheel. The chemical bond between filler alloy and CBN grains was achieved. The grinding wheel has excellent grinding performance for nickel-based superalloy Inconel718. Peng et al. [22] proposed a novel method of pressurized internal-cooling and fabricated a pressurized internal-cooling slotted grinding wheel with 3D printing. The results proved that this method had better heat transfer efficiency than that of conventional grinding. Lower grinding temperature and better workpiece surface quality were obtained.

In the grinding of nickel-based superalloys, many issues are faced such as high grinding temperature, low material removal rate, and poor surface integrity. From the viewpoint of the grinding mechanism analysis, this is contributed to the high normal grinding force and low tangential grinding force [23–25]. For some difficult-to-machine materials, the energy required for elastic and plastic deformation as well as material removal is quite huge during grinding [26, 27]. The normal grinding force of the difficult-to-machine materials is tens of times or even hundreds of times larger than that of the ordinary materials. Hence, it is important to increase tangential grinding force, reduce normal grinding force, and improve the ratio of tangential force to normal force for difficult-to-machine materials. However, current studies on the grinding force model and experimental investigation are still unable to change the fact of large normal grinding force and low tangential grinding force during grinding. Few studies are focused on how to reduce the grinding force and the ratio of the normal force to the tangential force in the grinding process.

In this work, we proposed a novel high-shear and low-pressure grinding method and developed a specially grinding tool made of flexible composites. The basic composition of the grinding tool and the grinding concept were introduced in detail. Grinding experiments on Inconel718 were carried out to investigate the grinding performance. Effects of wheel speed, workpiece speed, and grinding depth of cut on surface roughness were analyzed. The optimal parameters were obtained under the selected conditions. The surface roughness and micro-morphology of the Inconel718 workpieces were investigated. The grinding characteristics with the novel

grinding tool were explored through SEM observation and EDS analysis.

## 2 Introduction of the high-shear and low-pressure grinding method

As illustrated in Fig. 1, the novel grinding tool is consisted of two parts, i.e., grinding tool substrate and abrasive layer. The substrate material of the grinding tool was made of 304 stainless steel which owned enough rigidity and corrosion resistance. The abrasive layer was fabricated through flexible composites, i.e., the plain weave fabrics that were impregnated into micro/nano abrasive mixed shear thickening fluid (STF) [28, 29]. The composition of the abrasive layer mainly included abrasive particle (white fused alumina), high-performance fibers (Kevlar29), dispersed phase (nano-silica), dispersion medium (PEG), and other additives.

The machining concept of the high-shear and low-pressure grinding was introduced as the following three steps:

In step 1, the grinding tool starts to come into contact with the surface of the workpiece. The abrasive particles and the dispersed phase are uniformly dispersed in the dispersion medium of the abrasive layer. Moreover, the fibers are uniformly distributed, and the directivity is distinct.

In step 2, the abrasive layer of the grinding tool collides and squeezes with the micro-convex peak of the workpiece surface in the contact interface. The micro-convex peak generates a large reverse tangential load on the grains of the abrasive layer instantaneously under the condition of high relative motion. Meanwhile, the micro/nano grains in the contact area quickly produce “hydro-cluster effects” and form “particle clusters” [30]. The macroscopic viscosity of the STF around the grains increases sharply and tends to be stable. The “particle clusters” collides with the micro-convex peak of the workpiece surface. When the force exceeds the critical yield stress of the workpiece material, the micro-convex peak is removed by the grains in abrasive layer of the grinding tools.

In step 3, the “particle clusters” involved in the grinding process gradually disappears after the material is removed, and the reverse tangential load disappears. The grains and the dispersed phase become uniformly dispersed again in the dispersion medium. The grinding tool returns to the initial state. The high-shear and low-pressure grinding is achieved through recycling the three steps.

## 3 Experimental details

### 3.1 Experimental materials

The major chemical reagent, which were used in the study, included hydrophilic fumed silica (H-300) (BET specific

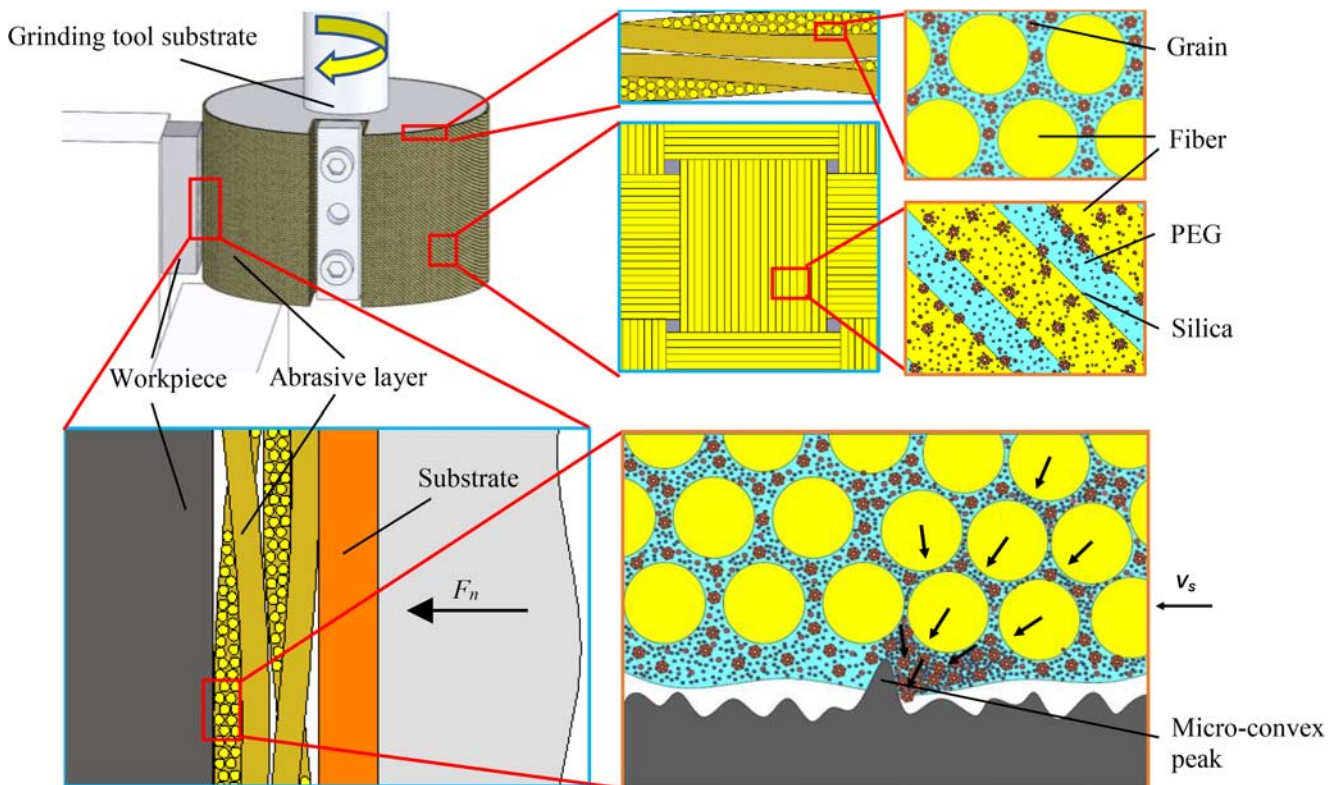


**Fig. 1** Microscopic diagram of high-shear and low-pressure grinding principle

surface area  $300 \text{ m}^2/\text{g}$ , primary particle size  $7\text{--}40 \text{ nm}$ ), polyethylene glycol (PEG-200, chemically pure, Newtonian fluid, viscosity of  $32 \text{ mPa s}$  under  $25 \text{ }^\circ\text{C}$ ), and ethyl alcohol absolute (mass fraction  $\geq 99.7\%$ , viscosity of  $1.074 \text{ mPa s}$  under  $20 \text{ }^\circ\text{C}$ ). The high-performance Kevlar29 was woven into plain weave fabric by a warp knitting interval ( $1500\text{D}$ ,  $200 \text{ g/m}^2$ ). White fused alumina ( $\text{Al}_2\text{O}_3$ ) with average particle size of  $6.5 \text{ }\mu\text{m}$  was selected as the abrasive in the experiments. The Inconel718 block was used as the workpiece. The main chemical composition of the workpiece was listed in Table 1.

### 3.2 Preparation and test of the abrasive layer

In this study, the solid content of  $\text{SiO}_2/\text{PEG}$  system in the shear thickening fluid (STF) was  $15 \text{ wt.}\%$  while the white fused alumina abrasive had a mass fraction of  $5 \text{ wt.}\%$  in the  $\text{SiO}_2/\text{PEG}/\text{Al}_2\text{O}_3$  system of the shear thickening abrasive fluid (STAF).

The abrasive layers, i.e., the flexible composites were prepared as the following procedure. The appropriate amount of

the fumed nano-silica and PEG-200 was weighed according to the ratio. The fumed nano-silica was sufficiently dispersed in PEG-200 to prepare the STF. The right amount of white fused alumina abrasive was weighed. After vacuum treatment for  $\text{SiO}_2/\text{PEG}$  system STF, the white fused alumina was dispersed in the STF to prepare the STAF. The STAF was diluted with ethanol (1:2). Then, the high-performance fiber fabrics were immersed in the diluted solution. The abrasive layer was finally obtained after drying. The prepared abrasive layer was mounted on the grinding tool substrate to fabricate the novel grinding tool. The SEM images of the fumed nano-silica and the white fused alumina selected in the experiment are respectively shown in Fig. 2a, b.

The rheological measurements of the prepared  $\text{SiO}_2/\text{PEG}$  system, i.e., STF and the  $\text{SiO}_2/\text{PEG}/\text{Al}_2\text{O}_3$  system, i.e., STAF were tested using an Aaton Paar Physica MCR302 rotary rheometer. The measurement fixture was a  $50\text{-mm}$  diameter parallel plate apparatus, and test temperature was kept at a constant temperature at  $25 \text{ }^\circ\text{C}$ . The relationship between viscosity and shear rate for the STF ( $15 \text{ wt}\%$   $\text{SiO}_2$  loading) and the STAF ( $15 \text{ wt}\%$  silica +  $5 \text{ wt}\%$   $\text{Al}_2\text{O}_3$  loading) was shown in Fig. 3.

As shown in Fig. 3, it was found that the prepared STF and the STAF have obvious shear thickening effects. With the increase of shear rate, STF and STAF disperse system exhibited three distinct viscosity changes: zone I, II, and III. Zone I and III were shear thinning zone in which the dispersion

**Table 1** Main chemical composition of Inconel718 workpiece

| Element | Ni    | Cr   | Fe    | Nb   | Mo   | Ti   | Al   | Cu   | Mn   | O    |
|---------|-------|------|-------|------|------|------|------|------|------|------|
| Wt%     | 50.26 | 20.3 | 18.49 | 3.31 | 2.89 | 1.41 | 0.61 | 0.54 | 0.46 | 0.28 |

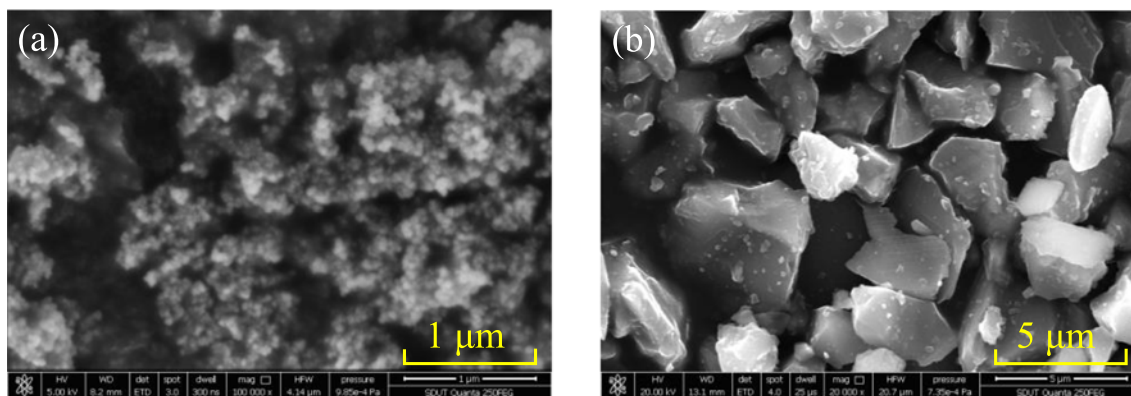


**Fig. 2** SEM images of **a** fumed nano-silica and **b** white fused alumina

exhibited a continuous decrease in viscosity, while zone II was a shear thickening zone where the dispersion exhibited a sharp increase in viscosity and produce “hydro-cluster effects” to form “particle clusters” in micro/nano scale. The maximum shear thickening viscosity was 310.67 Pa s for STF while it is 68.03 Pa s for STAF.

Figure 4 shows the SEM images of neat Kevlar, Kevlar/STF composite, and the Kevlar/STF/ $\text{Al}_2\text{O}_3$  abrasive layer. It was seen that the neat Kevlar29 plain weave fabric had good fiber direction and smooth surface. There were no fiber damages as shown in Fig. 4a. As for Kevlar/STF composite, the Kevlar29 fiber was attached with a large amount of fumed nano-silica particles. Meanwhile, there were sufficient STFs between fibers as exhibited in Fig. 4b. This was able to contribute to shear thickening effects during grinding. As shown in Fig. 4c, there were a large number of fumed nano-silica particles and #2000  $\text{Al}_2\text{O}_3$  abrasive attached to the fiber surface of the STAF abrasive layer. Through optimizing the shear thickening effects, the fumed nano-silica particles were coated with  $\text{Al}_2\text{O}_3$  grains to generate “hydro-cluster effects” to remove the micro-convex peaks on the surface of the workpiece.

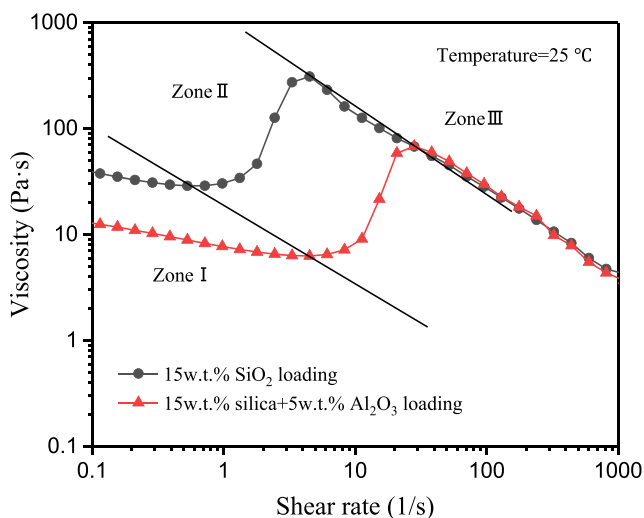


**Fig. 3** Rheological behavior of pure shear thickening fluid with **a** 15 wt%  $\text{SiO}_2$  loading and **b** 15 wt% silica + 5 wt%  $\text{Al}_2\text{O}_3$  loading

### 3.3 Experimental setup and conditions

High-shear and low-pressure grinding experiments of the Inconel718 workpiece were conducted on a CNC center as shown in Fig. 5. The CNC center (VKN640) was equipped with a positioning resolution of 5  $\mu\text{m}$  in X-, Y-, and Z-axes. The developed novel grinding tool was installed on the spindle of the CNC center. The workpiece was connected to the precision vice. The surface topography and elemental variation of the workpieces were measured by the Quanta 250 field emission scanning electron microscopy. The surface topography of the workpieces was characterized using a metalloscope (Axio Lab A1, Germany). The surface roughness was measured with the TR 200 rough meter before and after grinding. Five times in the chosen area were measured. The average value of the five measurements was taken as the surface roughness value of the area. Sampling length of the measurement was 0.8 mm. Assessment length was 4.0 mm.

The dimension of the Inconel718 workpiece is 10 mm (length)  $\times$  7 mm (width)  $\times$  3 mm (height). The surface pre-treatment was performed with a 60 # alumina wheel (grit size 250  $\mu\text{m}$ ) to obtain a uniform surface with an initial surface roughness of  $\sim$  500 nm prior to the grinding experiments. The experimental conditions were listed in Table 2. In the grinding tests, the effects of grinding wheel speed were first explored. Then, the optimal workpiece speed was further conducted under the optimal wheel speed. Finally, the optimal wheel speed and the workpiece speed as prerequisite were selected to investigate the effects of the grinding depth of cut on the grinding performance.

## 4 Experiments and discussion

### 4.1 Surface roughness

The influencing factors studied for the grinding experiments are wheel speed, workpiece speed, and grinding depth of cut. The whole grinding process consisted of 240 grinding cycles.

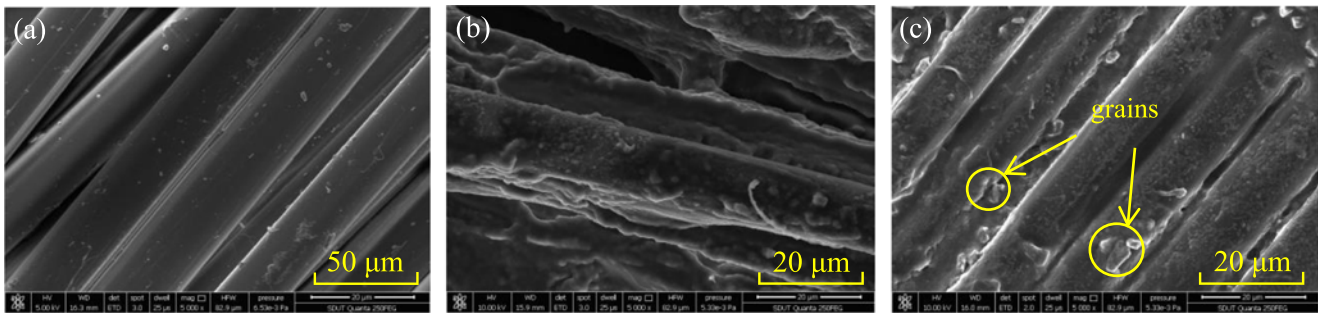


Fig. 4 SEM images of **a** neat Kevlar, **b** Kevlar/STF composite, and **c** Kevlar/STF/Al<sub>2</sub>O<sub>3</sub> abrasive layer

The grinding wheel passed through the workpiece surface once for one grinding cycle. The effects of wheel speed, workpiece speed, and grinding depth of cut on the surface roughness of Inconel718 workpiece were investigated. The optimal process parameters were obtained under the selected conditions.

Figure 6 shows surface roughness variation versus wheel speed when the workpiece speed was selected as 2000 mm/min, and the grinding depth of cut was fixed at 180 μm. The results showed that surface roughness values *Ra* of 153.0 nm, 178.6 nm, and 249.4 nm were correspondingly obtained at the wheel speed of 1 m/s, 2 m/s, and 3 m/s. It was seen that the best grinding performance was attained when the wheel speed was selected as 1 m/s, followed by 2 m/s and 3 m/s. The surface roughness reduced from *Ra* 473.7 nm to *Ra* 153 nm at the wheel speed of 1 m/s after 240 grinding cycles. The value of surface roughness was reduced by 68%. It was found that the surface roughness of Inconel718 workpiece increased

with the increase of the wheel speed. This was attributed to the decreases of the viscosity of STAF with wheel speed increasing. The holding force of the grains reduced on the novel grinding tool.

Figure 7 shows the effects of workpiece speed on the ground surface roughness at the wheel speed of 1 m/s and the grinding depth of 180 μm. The workpiece speed of 2000 mm/min, 6000 mm/min, and 10,000 mm/min were respectively adopted. The corresponding surface roughness *Ra* of 150.3 nm, 242.8 nm, and 342.6 nm was attained after 240 grinding cycles. It was obviously found that the surface quality of the Inconel718 workpiece was inversely proportional to the workpiece speed, as shown in Fig. 7. As the relative processing time of the grinding tool on the workpiece surface becomes short at the large feed speed, the grinding surface quality becomes poor.

In order to further investigate the effects of grinding depth of cut on the surface roughness, the grinding depth of cut was

Fig. 5 Grinding setup

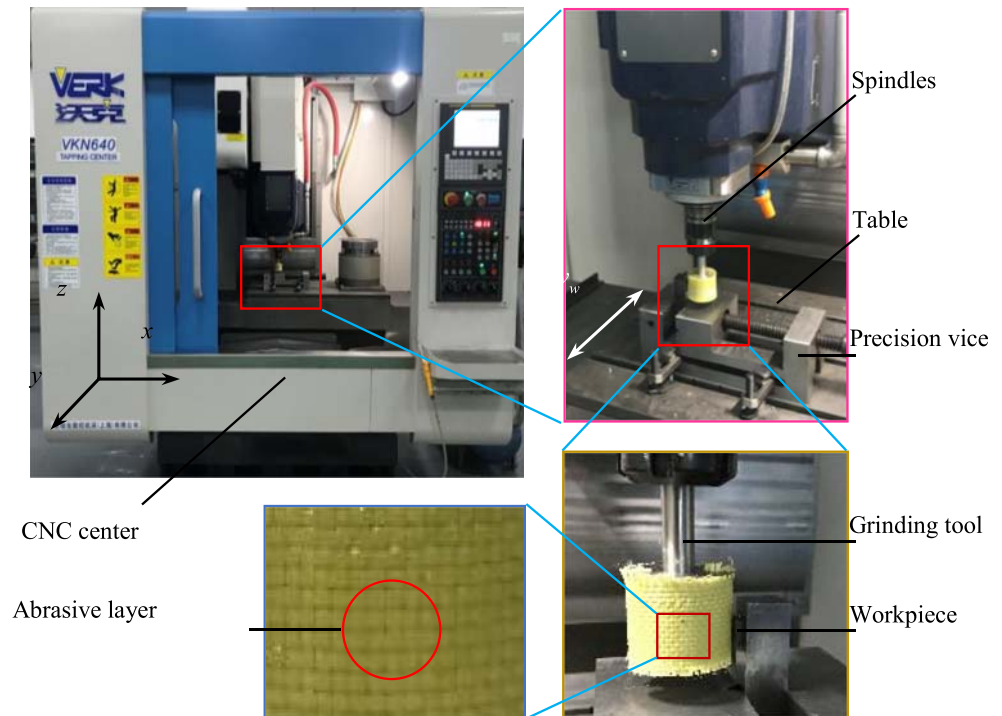


**Table 2** Experimental conditions

| Items                                   | Parameters         |
|---|--------------------|
| Workpiece material                      | Inconel718         |
| Initial roughness (nm)                  | $Ra \sim 500$      |
| Wheel speed (m/s)                       | 1, 2, 3            |
| Workpiece speed (mm/min)                | 2000, 6000, 10,000 |
| Grinding depth of cut ( $\mu\text{m}$ ) | 120, 150, 180      |

set as 120  $\mu\text{m}$ , 150  $\mu\text{m}$ , and 180  $\mu\text{m}$ , respectively. The grinding wheel speed of 1 m/s and workpiece speed of 2000 mm/min were fixed during the grinding tests. As shown in Fig. 8, the surface roughness slightly decreased with the increase of the grinding cycles when the grinding depth was selected as 120  $\mu\text{m}$ . The surface roughness ( $Ra$ ) only reduced to 419.8 nm from the initial 495.0 nm after 240 grinding cycles. However, the value of surface roughness of the Inconel718 workpiece decreased with grinding depth increasing. In particular, the value of surface reduced down to 150 nm at the grinding depth of cut of 180  $\mu\text{m}$  only after 120 grinding cycles. The value of surface roughness was the lowest at the grinding depth of cut of 180  $\mu\text{m}$ , followed by that at the grinding depth of cut of 250  $\mu\text{m}$  and 120  $\mu\text{m}$ , respectively. This grinding characteristic with the novel grinding tool was opposite to that of the conventional grinding wheel. The reason is due to high elasticity for the flexible composited tool. The contact area between the tool and the workpiece became large with the increase of grinding depth of cut. The cutting behavior of each active grain enhanced accordingly.

As observed from Figs. 6, 7, and 8, it can be concluded that the grinding depth of cut has the most significant influence on surface roughness of the workpiece after grinding, while the

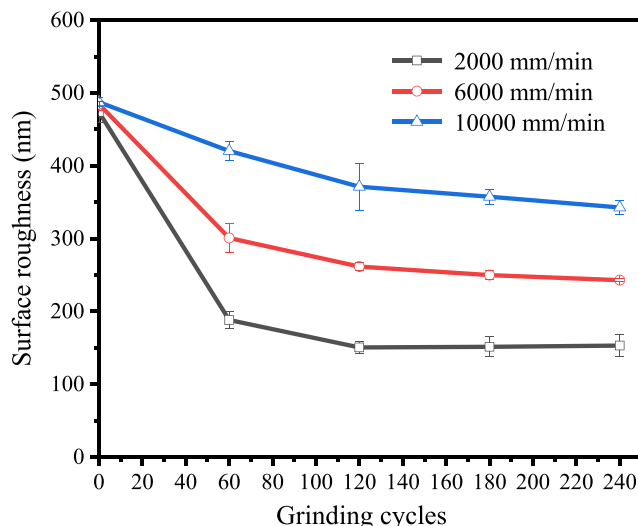


**Fig. 7** Surface roughness variation versus workpiece speed

wheel speed has the least significant influence on the surface roughness. The surface roughness of the workpiece greatly reduced after 60 grinding cycles, whereas it became stable after 120 grinding cycles. This indicated that the material removal behavior was substantially completed during the first 60 grinding cycles. In the subsequent 60 grinding cycles, the surface roughness slightly decreased due to the rigidity of machine and the elasticity of the grinding tool. In addition, the number of micro-convex peaks on the surface reduced due to the removal of the workpiece material. This caused a negative impact on the grinding performance of the novel grinding tools. Within the grinding parameters selected, the optimal parameters were concluded as wheel speed of 1 m/s, workpiece speed of 2000 mm/min, and grinding depth of cut of 180  $\mu\text{m}$ .

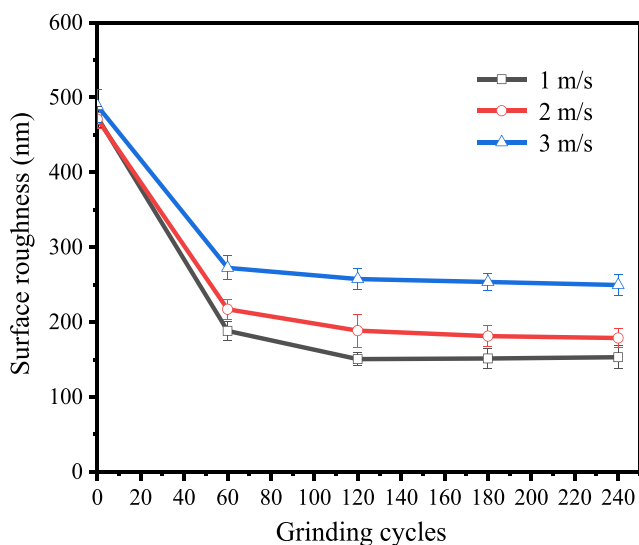


**Fig. 6** Surface roughness variation versus wheel speed

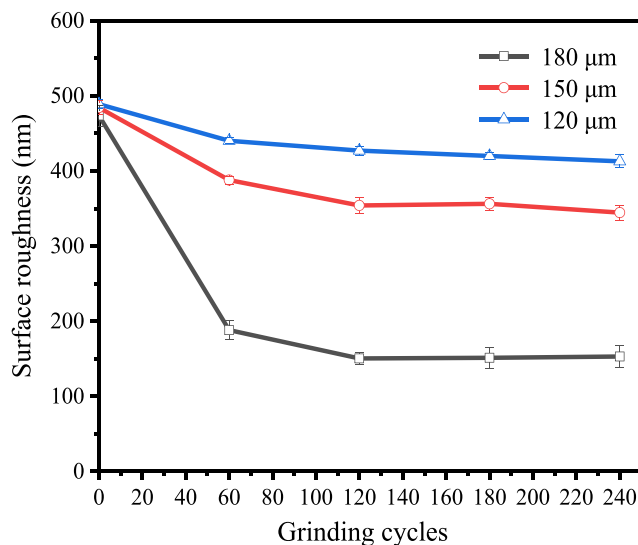


**Fig. 8** Surface roughness variation versus depth of cut

## 4.2 Surface topography

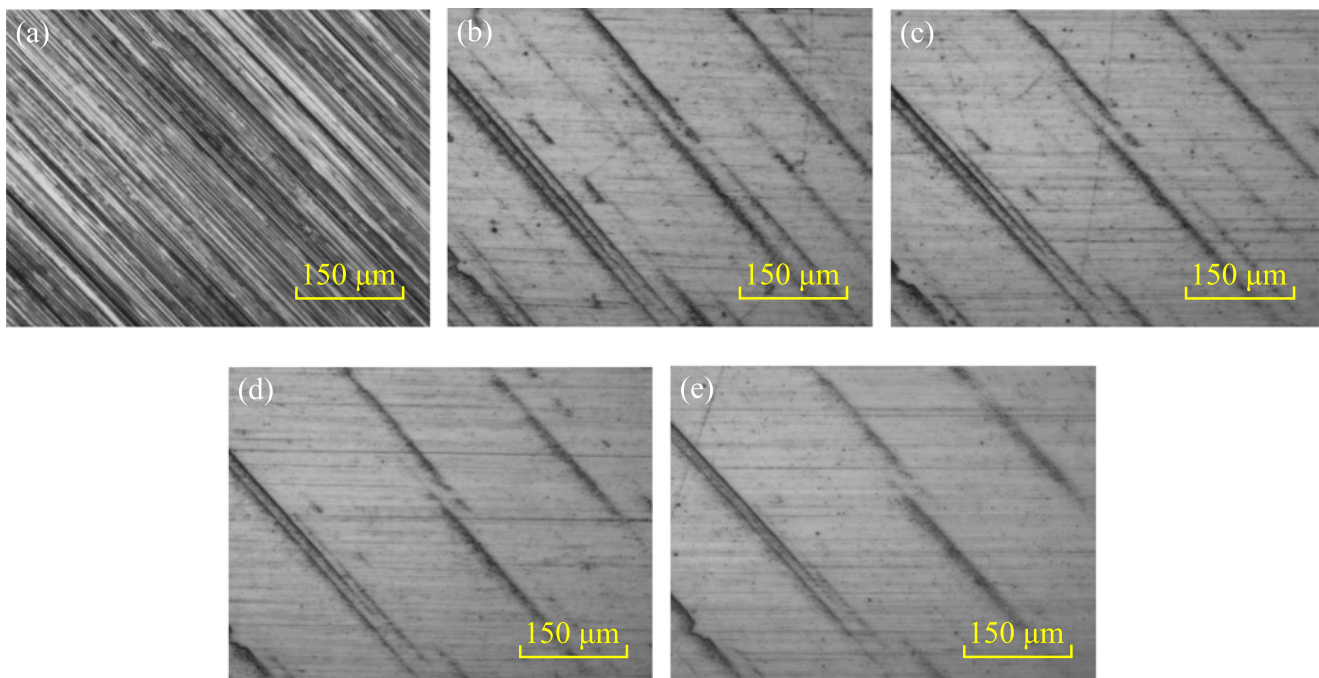
The surface morphology of the ground Inconel718 workpiece was investigated under the optimal grinding parameters. The workpiece surface was observed using a metalloscope (Axio Lab A1, Germany) before and after grinding. The magnification of the metalloscope was chosen as 200 times. Figure 9 shows the specifically area micro-morphology of the Inconel718 workpiece at each 60 grinding cycles. The surface of the workpiece exhibited obvious pre-treatment textures by grinding with the conventional wheel in Fig. 9a. The surface texture by pretreatment was obvious. There were serious surface defects on the surface. As shown in Fig. 9b, the grinding texture generated by the pretreatment substantially disappeared after 60 grinding cycles, leaving only a small amount of deep scratches. As shown in Fig. 9c–e, the marks of deep scratches gradually became shallow with the increase of the grinding cycles. However, the grinding textures with the novel grinding tool became visible as the grinding cycles increased.

In order to understand the surface characteristics of the workpiece, field-emission scanning electron microscopy (Quanta 250) was employed to further characterize the surface of the workpiece before and after grinding with the novel grinding tool. The workpiece was ultrasonically cleaned with ethanol prior to observation. Figure 10 shows the surface micro-morphology of the Inconel718 workpiece before and after grinding. The ground workpiece had undergone 240 grinding cycles. As shown in Fig. 10a, the surface obtained by pretreatment with a conventional alumina wheel (grit size

250  $\mu\text{m}$ ) had a large number of grinding textures and surface defects. The scratches produced by the grinding were different in depth and width due to different protrusion heights of abrasive grains on the surface of the conventional grinding wheel. As shown in Fig. 10b, after 240 grinding cycles with the novel grinding tool, the original scratches, pits, and other defects on the surface of the workpiece disappeared, only leaving a small amount of original deep scratches on the surface. The marks of deep scratches had also become very shallow. This resulted in the generation of new surface with good surface quality. The depth of the new created grinding texture was shallower. The width of the texture was smaller as well. The main reason was caused by small particle size (grit size 6.5  $\mu\text{m}$ ). The holding strength of the “particle clusters” was also limited in the developed novel grinding wheel. Hence, the equivalent grinding thickness of the single grain was small. The result showed that the novel grinding tool had a good processing performance on the Inconel718 superalloy although there were residual deep pretreatment textures on the surface of the workpiece.

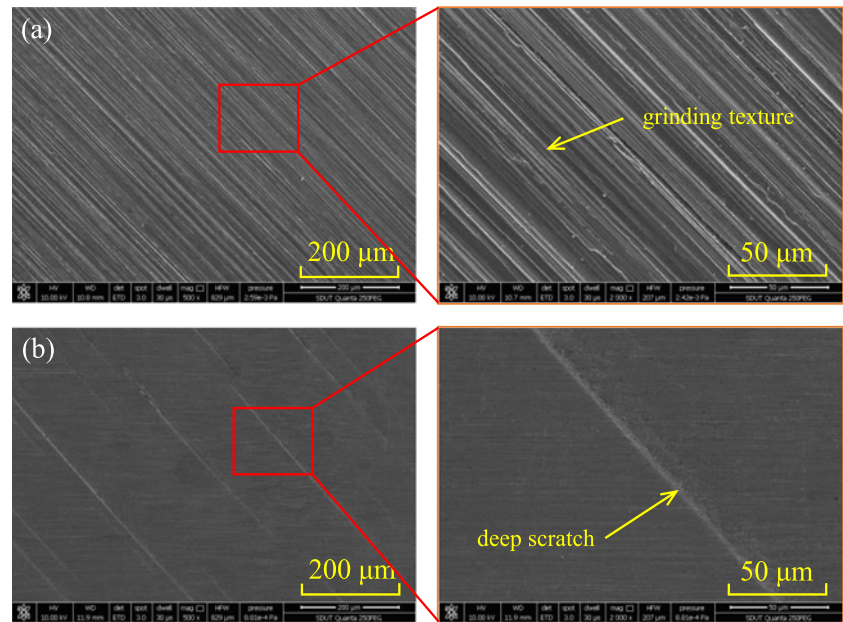
## 4.3 Elemental change analysis

Figure 11 shows the SEM images of the Inconel718 workpiece and the abrasive layer before and after 240 grinding cycles under the optimal grinding parameters. The EDS analysis results are shown in Fig. 12. The areas of red rectangles shown in Fig. 11a–d are corresponding to the EDS analysis results of Fig. 12a–d. As shown in Fig. 11a, b, the defects like the corrugated pits on the surface of the workpiece were



**Fig. 9** Surface topography of Inconel718 workpiece using the developed grinding tool grinding tool during grinding process **a** before grinding, **b** after 60 grinding cycles, **c** after 120 grinding cycles, **d** after 180 grinding cycles, and **e** after 240 grinding cycles

**Fig. 10** SEM image of workpiece with before and after grinding. **a** before grinding and **b** after grinding



substantially eliminated. The elemental analysis of the Inconel718 workpieces before and after grinding is shown in Fig. 12a, b. The main elements of Inconel718 were detected as Ni, Cr, Fe, Nb, Mo, O, Al, and Ti on the workpiece surface. The compositions of the main elements were basically unchanged before and after grinding. There were no large amounts of element diffusion phenomena and abrasive ingredient adhesion on the surface of the workpiece. As shown in Fig. 11c, the surface of the grinding tool was smooth, and the fiber direction was consistent before grinding. The surface has been adhered by a large amount of STAF. However, after grinding, the surface of the grinding tool was slightly worn and broken for several fibers as shown in Fig. 11d. The overall

worn status was not very serious. It was observed that STAF had a large amount of flocculation due to shear thickening effects. Elemental analysis of the abrasive layer before and after grinding was respectively shown in Fig. 12c, d. Before grinding, the main elements, i.e. O, C, Si, and Al, were detected on the surface of the abrasive layer. However, after grinding, it appeared a large amount of the main elements of Inconel718 such as Ni, Cr, and Fe. It was found that the Al element was slightly lost. The reason for the elemental change was contributed to adhesion of the worn Inconel718 debris onto the surface of the abrasive layer after grinding. As the novel grinding tool was not bonded, there was a little grain loss during the grinding.

**Fig. 11** SEM images of Inconel718 **a** before grinding and **b** after grinding. SEM images of abrasive layer **c** before grinding and **d** after grinding

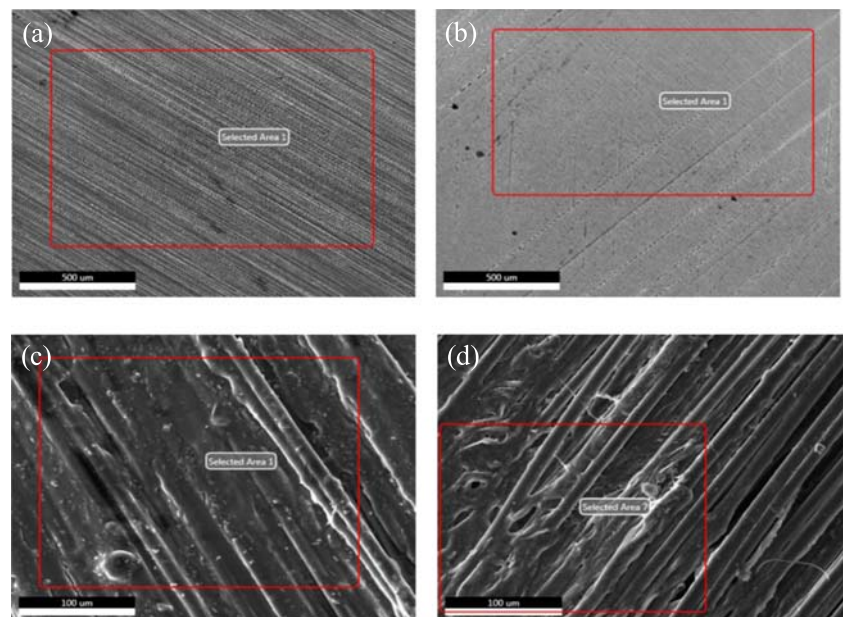
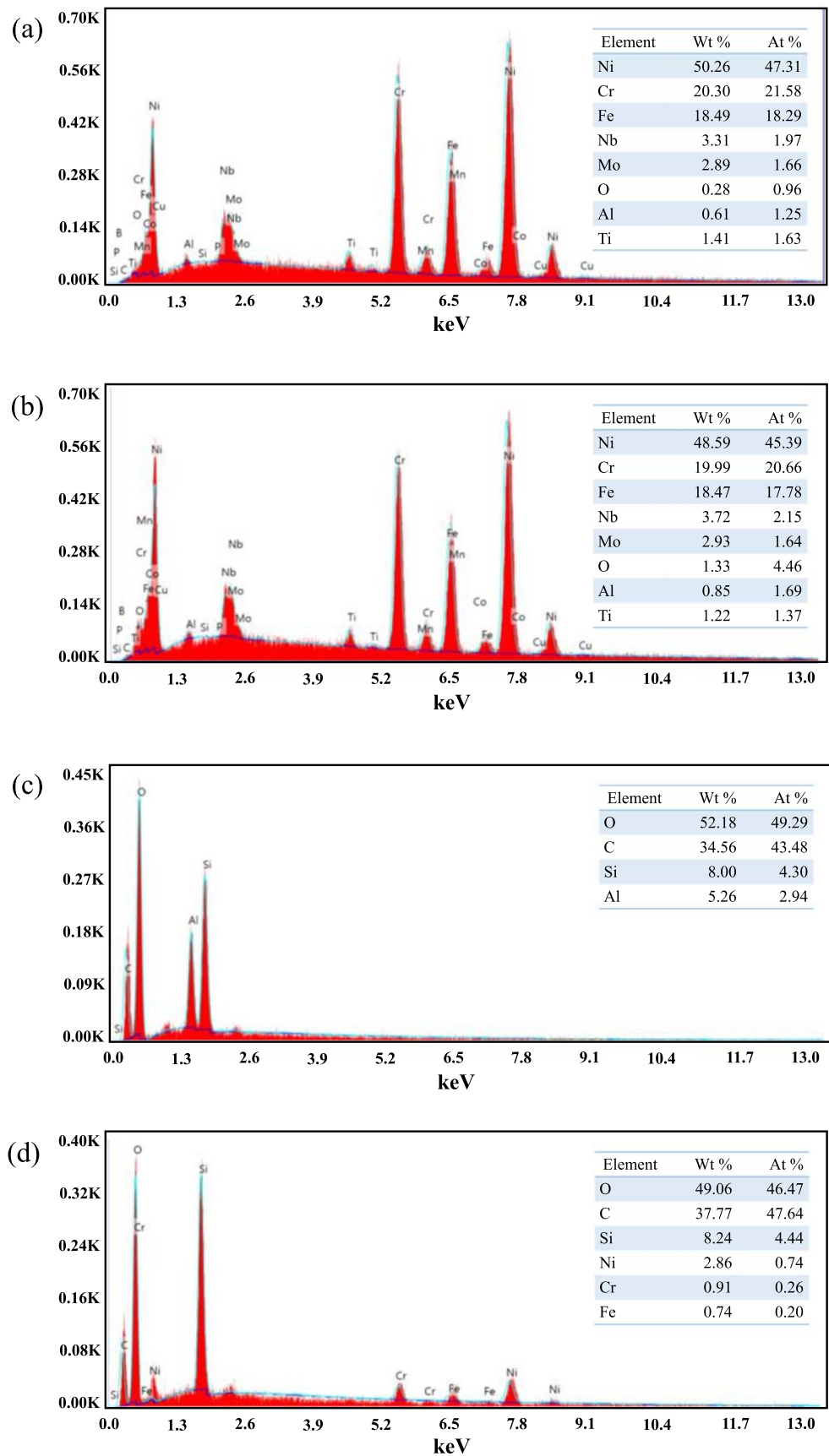




**Fig. 12** EDS results of Inconel718 workpiece **a** before grinding **b** after grinding. EDS results of the abrasive layer **c** before grinding and **d** after grinding



## 5 Conclusions

A novel high-shear and low-pressure grinding method was proposed in this work. A novel grinding tool made of flexible composites was designed and developed. In order to explore the fundamental grinding characteristics and material removal mechanism, the grinding experiments were carried out on the Inconel718 superalloy with the developed grinding tool. The effects of grinding parameters on surface roughness, surface morphology, and elemental change were investigated. The results obtained can be summarized as follows:

- (1). The measured rheological behavior for both STF and STAF showed that the two fluids owned significant shear thickening characteristics. The maximum shear thickening viscosity of the STF and STAF were 310.67 Pa s and 68.03 Pa s, respectively. In the abrasive layer of the flexible composited tool, the STAF was uniformly distributed among the fibers.
- (2). The grinding results showed that the optimal grinding parameters were wheel speed of 1 m/s, workpiece speed of 2000 mm/min, and grinding depth of cut of 180  $\mu\text{m}$  under the grinding conditions selected. The surface roughness ( $R_a$ ) of the Inconel718 workpiece reduced from 473.7 nm to 153.0 nm under the optimal parameters.
- (3). The original grinding textures generated by pretreatment were almost eliminated after high-shear and low-pressure grinding with the novel grinding wheel. The ground Inconel718 workpiece became quite smooth while the shallow marks generated as the grinding cycles increased.
- (4). Through EDS analysis, there was no large amount of element diffusion and abrasive ingredient adhesion on the workpiece surface. There were residual worn debris attached to the surface of the novel grinding tool, whereas the tool still sustained a good condition. In addition, it was found that there was a little loss of grains for the novel grinding tool after 240 grinding cycles.

**Acknowledgments** The authors gratefully acknowledge financial supports by the National Natural Science Foundation of China (Grant No. 51875329 and 51905322), Taishan Scholar Special Foundation of Shandong Province (tsqn201812064), Shandong Provincial Natural Science Foundation, P.R. China (Grant No. ZR2017MEE050), Shandong Provincial Key Research and Development Project, P.R. China (Grants No. 2018GGX103008), Scientific Innovation Project for Young Scientists in Shandong Provincial Universities, China (Grant No. 2019KJB030), and Key Research and Development Project of Zibo City, China (Grant No. 2019ZBXC070).

## References

1. Wang PZ, He ZS, Zhang YX, Zhao SS (2017) Control of grinding surface residual stress of Inconel718. *Procedia Eng* 174:504–511. <https://doi.org/10.1016/j.proeng.2017.01.174>
2. Lu HJ, Jia XC, Zhang KF, Yao CJ (2002) Fine-grained pretreatment process and superplasticity for INCONEL718 superalloy. *Mater Sci Eng A* 326(2):382–385. [https://doi.org/10.1016/S0921-5093\(01\)01521-0](https://doi.org/10.1016/S0921-5093(01)01521-0)
3. Tso PL (1995) Study on the grinding of Inconel718. *J Mater Process Technol* 55(3):421–426. [https://doi.org/10.1016/0924-0136\(95\)02026-8](https://doi.org/10.1016/0924-0136(95)02026-8)
4. Li Q, Gong YD, Cai M, Liu MJ (2017) Research on surface integrity in milling inconel718 superalloy. *Int J Adv Manuf Technol* 92(1–4):1449–1463. <https://doi.org/10.1007/s00170-017-0080-0>
5. Hood R, Soo SL, Aspinwall DK, Mantle AL (2018) Tool life and workpiece surface integrity when turning an RR1000 nickel-based superalloy. *Int J Adv Manuf Technol* 98(9–12):2461–2468. <https://doi.org/10.1007/s00170-018-2371-5>
6. Chen M, Sun FH, Lee YM, Yang SH (2004) Surface quality studies with respect to grinding burn of new typical nickel-based superalloy. *Key Eng Mater* 259-260:233–238. <https://doi.org/10.4028/www.scientific.net/KEM.259-260.233>
7. Tian YB, Liu F, Wang Y, Wu H (2017) Development of portable power monitoring system and grinding analytical tool. *J Manuf Process* 27:188–197. <https://doi.org/10.1016/j.jmapro.2017.05.002>
8. Wu CJ, Li BZ, Liu Y, Liang SY (2017) Surface roughness modeling for grinding of silicon carbide ceramics considering co-existence of brittleness and ductility. *Int J Mech Sci* 133:167–177. <https://doi.org/10.1016/j.ijmecsci.2017.07.061>
9. Godino L, Pombo I, Sanchez JA, Alvarez J (2018) On the development and evolution of wear flats in microcrystalline sintered alumina grinding wheels. *J Manuf Process* 32:494–505. <https://doi.org/10.1016/j.jmapro.2018.03.023>
10. Tian YB, Zhong ZW, Rawat R (2015) Comparative study on grinding of thin-walled and honeycomb-structured components with two CBN wheels. *Int J Adv Manuf Technol* 81(5–8):1097–1108. <https://doi.org/10.1007/s00170-015-7114-2>
11. Agarwal S, Rao PV (2010) Grinding characteristics, material removal and damage formation mechanisms in high removal rate grinding of silicon carbide. *Int J Mach Tools Manuf* 50(12):1077–1087. <https://doi.org/10.1016/j.ijmachtools.2010.08.008>
12. Sinha MK, Setti D, Ghosh S, Rao PV (2016) An investigation on surface burn during grinding of Inconel718. *J Manuf Process* 21:124–133. <https://doi.org/10.1016/j.jmapro.2015.12.004>
13. Dai CW, Ding WF, Zhu YJ, Xu JH, Yu HW (2017) Grinding temperature and power consumption in high speed grinding of Inconel718 nickel-based superalloy with a vitrified CBN wheel. *Precis Eng* 52:192–200. <https://doi.org/10.1016/j.precisioneng.2017.12.005>
14. Dai CW, Ding WF, Xu JH, Xu XP, Fu DK (2016) Effects of undeformed chip thickness on grinding temperature and burn-out in high-efficiency deep grinding of inconel718 superalloys. *Int J Adv Manuf Technol* 89(5–8):1841–1852. <https://doi.org/10.1007/s00170-016-9192-1>
15. Dai CW, Yu TY, Ding WF, Xu JH, Yin Z, Li H (2019) Single diamond grain cutting-edges morphology effect on grinding mechanism of Inconel718. *Precis Eng* 55:119–126. <https://doi.org/10.1016/j.precisioneng.2018.08.017>
16. Bhaduri D, Soo SL, Aspinwall DK, Novovic D, Martin D (2012) A study on ultrasonic assisted creep feed grinding of nickel-based superalloys. *Procedia CIRP* 1:359–364. <https://doi.org/10.1016/j.procir.2012.04.064>
17. Yao CF, Jin QC, Huang XC, Wu DX (2013) Research on surface integrity of grinding inconel718. *Int J Adv Manuf Technol* 65(5–8):1019–1030. <https://doi.org/10.1007/s00170-012-4236-7>
18. Gong YD, Zhou YG, Wen XL, Cheng J, Sun Y, Ma LJ (2017) Experimental study on micro-grinding force and subsurface microstructure of nickel-based single crystal superalloy in micro grinding. *J Mech Sci Technol* 31(7):3397–3410. <https://doi.org/10.1007/s12206-017-0629-8>

19. Li QL, Xu JH, Su HY, Lei WN (2015) Fabrication and performance of monolayer brazed CBN wheel for high-speed grinding of super-alloy. *Int J Adv Manuf Technol* 80(5–8):1173–1180. <https://doi.org/10.1007/s00170-015-7125-z>
20. Li HN, Axinte D (2016) Textured grinding wheels: a review. *Int J Mach Tool Manu* 109:8–35. <https://doi.org/10.1016/j.ijmactools.2016.07.001>
21. Mohamed AMO, Bauer R, Warkentin A (2014) A novel method for grooving and re-grooving aluminum oxide grinding wheels. *Int J Adv Manuf Technol* 73(5–8):715–725. <https://doi.org/10.1007/s00170-014-5880-x>
22. Peng RT, Huang XF, Tang XZ, Chen R, Hu YB (2018) Performance of a pressurized internal-cooling slotted grinding wheel system. *Int J Adv Manuf Technol* 94(5–8):1–16. <https://doi.org/10.1007/s00170-017-1014-6>
23. Durgumahanti USP, Singh V, Rao PV (2010) A new model for grinding force prediction and analysis. *Int J Mach Tools Manuf* 50(3):231–240. <https://doi.org/10.1016/j.ijmactools.2009.12.004>
24. Nguyen T, Zhang LC (2009) Performance of a new segmented grinding wheel system. *Int J Mach Tools Manuf* 49(3–4):291–296. <https://doi.org/10.1016/j.ijmactools.2008.10.015>
25. Malkin S (1991) Grinding technology: theory and applications of machining with abrasives. *Int J Mach Tools Manuf* 31(3):435–436. [https://doi.org/10.1016/0890-6955\(91\)90088-K](https://doi.org/10.1016/0890-6955(91)90088-K)
26. Zhang DK, Li CH, Zhang YB, Jia DZ, Zhang XW (2015) Experimental research on the energy ratio coefficient and specific grinding energy in nanoparticle jet mql grinding. *Int J Adv Manuf Technol* 78(5–8):1275–1288. <https://doi.org/10.1007/s00170-014-6722-6>
27. Masoumi H, Safavi SM, Salehi M (2014) Grinding force, specific energy and material removal mechanism in grinding of hvof-sprayed wc–co–cr coating. *Mater Manuf Process* 29(3):321–330. <https://doi.org/10.1080/10426914.2013.872261>
28. He QY, Cao SS, Wang YP, Xuan SH, Wang PF, Gong XL (2018) Impact resistance of shear thickening fluid/Kevlar composite treated with shear-stiffening gel. *Compos A Appl Sci Manuf* 106:82–90. <https://doi.org/10.1016/j.compositesa.2017.12.019>
29. Gürgen S, Li WH, Kuşhan MC (2016) The rheology of shear thickening fluids with various ceramic particle additives. *Mater Des* 104:312–319. <https://doi.org/10.1016/j.matdes.2016.05.055>
30. Li M, Lyu BH, Yuan JL, Dong CC, Dai WT (2015) Shear-thickening polishing method. *Int J Mach Tools Manuf* 94:88–99. <https://doi.org/10.1016/j.ijmactools.2015.04.010>

**Publisher's note** Springer Nature remains neutral with regard to jurisdictional claims in published maps and institutional affiliations.